nature nanotechnology

LETTERS

PUBLISHED ONLINE: 15 DECEMBER 2013 | DOI: 10.1038/NNANO.2013.272

Efficient solar water-splitting using a nanocrystalline CoO photocatalyst

Longb Liao[1], Qiuhui Zhang[1,2], Zhihua Su[1], Zhongzheng Zhao[3], Yanan Wang[1], Yang Li[1], Xiaoxiang Lu[1], Dongguang Wei[4], Guoying Feng[2], Qingkai Yu[5], Xiaojun Cai[6], Jimin Zhao[7], Zhifeng Ren[8], Hui Fang[9], Francisco Robles-Hernandez[10], Steven Baldelli[6] and Jiming Bao[1,3,6]*

The generation of hydrogen from water using sunlight could potentially form the basis of a clean and renewable source of energy. Various water-splitting methods have been investigated previously[1–8], but the use of photocatalysts to split water into stoichiometric amounts of H_2 and O_2 (overall water splitting) without the use of external bias or sacrificial reagents is of particular interest because of its simplicity and potential low cost of operation[1–4]. However, despite progress in the past decade, semiconductor water-splitting photocatalysts (such as $(Ga_{1-x}Zn_x)(N_{1-x}O_x)$) do not exhibit good activity beyond 440 nm (refs 1,2,9) and water-splitting devices that can harvest visible light typically have a low solar-to-hydrogen efficiency of around 0.1%[6,7]. Here we show that cobalt(II) oxide (CoO) nanoparticles can carry out overall water splitting with a solar-to-hydrogen efficiency of around 5%. The photocatalysts were synthesized from non-active CoO micropowders using two distinct methods (femtosecond laser ablation and mechanical ball milling), and the CoO nanoparticles that result can decompose pure water under visible-light irradiation without any co-catalysts or sacrificial reagents. Using electrochemical impedance spectroscopy, we show that the high photocatalytic activity of the nanoparticles arises from a significant shift in the position of the band edge of the material.

Femtosecond laser ablation and mechanical ball milling provide two clean physical processes to prepare CoO nanoparticles from CoO micropowders (see Supplementary Information for details on the synthesis of the nanoparticles). The nanoparticles fabricated from these methods exhibit very similar properties, and we therefore do not distinguish between them in the main text of the paper (exact contributions from the different techniques are clarified in the Supplementary Information). The nanoparticles were characterized with transmission electron microscopy (TEM), selective area electron diffraction (SAED), and X-ray diffraction and X-ray photoemission spectra (XPS). The TEM image in Fig. 1a indicates that the average particle size is less than 10 nm. The SAED pattern in Fig. 1b and X-ray diffraction spectra in Supplementary Fig. 4 reveal the cubic lattice structure of CoO nanoparticles[10–12]. A high crystal quality of nanoparticles is confirmed by clear lattice fringes in the high-resolution TEM image shown in Supplementary Fig. 2. Figure 1c shows the Co 2*p* XPS of CoO nanoparticles and Co_3O_4 micropowders; two relatively stronger satellite features with respect to $2p_{3/2}$ and $2p_{1/2}$ in nanoparticles further confirm their CoO chemical nature[12–15]. No Co atoms or clusters can exist inside or on the surfaces of CoO nanoparticles because reduced metallic Co cannot be produced during the thermal decomposition of Co_3O_4 powders under the conditions described in the Supplementary Information.

Water-splitting experiments were performed in air-tight flasks with CoO nanoparticles suspended in neutral water. The nanoparticle suspension was illuminated through the bottom of the flask using either a 532 nm solid-state laser or an AM1.5G solar simulator (Newport 91160). The generated hydrogen and oxygen were sampled by a syringe (Gastight) and measured by a gas chromatograph (GC) equipped with a thermal conduction detector (GowMac). A mass spectrometer (SRS residue gas analyser, RGA200) was also used to identify isotope gas species from water splitting.

The first sign of overall water splitting is revealed by a typical GC trace, as shown in Fig. 2a. Not only were both H_2 and O_2 generated simultaneously, but also the H_2 to O_2 ratio was very close to the expected 2:1 stoichiometry. The very weak N_2 GC signal indicates that the reaction flask was air tight, and O_2 from air background is negligible. An essential qualification for photocatalytic reaction is that the reaction rate must depend on the light intensity[16]. This is, indeed, the case. As shown in Fig. 2b, no H_2 and O_2 could be observed when the system was kept in the dark. The production of H_2 and O_2 increased as the intensity of incident light increased. Again, a nearly 2:1 ratio of H_2 to O_2 was observed.

A photocatalytic water-splitting requires that the oxygen comes from the water instead of CoO. To identify the origin of the oxygen, we employed water labelled with ^{18}O isotope (Cambridge Isotope, 97%) in the experiment. We also developed a system based on a mass spectrometer to identify and quantify isotope gas species (see the Supplementary Information for details). Figure 2c shows partial pressure evolutions of H_2 and $^{36}O_2$ when a gas sample (1 ml) from the reaction flask was injected into a small vacuum chamber connected to the mass spectrometer: fast increases in the gas partial pressures were observed for both H_2 and $^{36}O_2$. In contrast, no detectable change for $^{36}O_2$ was observed when air (1 ml) was injected (lower curves in Fig. 2c). This observation is strong evidence that the generated oxygen comes from the isotope-labelled water. The H_2 RGA response from the injection of air is not caused by a high concentration of H_2 in the injected air (for further discussion see the Supplementary Information). To determine quantitatively the ratio of H_2 to $^{36}O_2$ from the RGA

[1]Department of Electrical & Computer Engineering, University of Houston, Houston, Texas 77204, USA, [2]College of Electronics & Information Engineering, Sichuan University, Chengdu 610064, China, [3]Materials Engineering Program, University of Houston, Houston, Texas 77204, USA, [4]Carl Zeiss Microscopy, LLC, One Zeiss Drive, Thornwood, New York 10594, USA, [5]Ingram School of Engineering, and Materials Science, Engineering and Commercialization, Texas State University, San Marcos, TX 78666, USA, [6]Department of Chemistry, University of Houston, Houston, Texas 77204, USA, [7]Institute of Physics, Chinese Academy of Sciences, Beijing 100190, China, [8]Department of Physics, University of Houston, Houston, Texas 77204, USA, [9]Department of Physics, Sam Houston State University, Huntsville, Texas 77341, USA, [10]College of Engineering Technology, University of Houston, Houston, Texas 77204, USA.
*e-mail: jbao@uh.edu

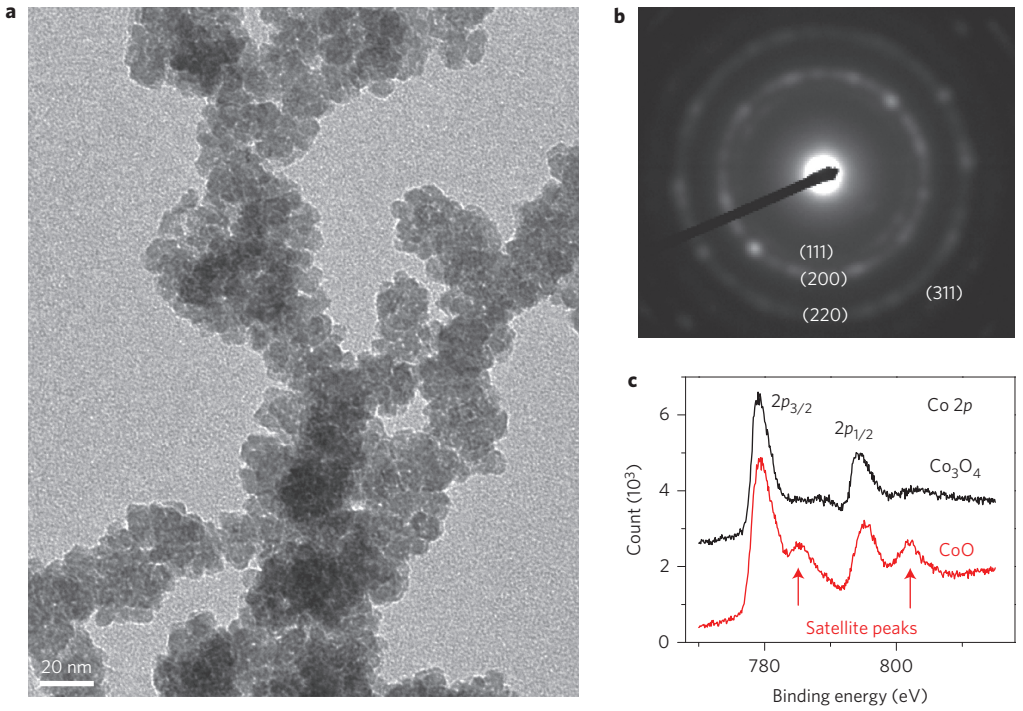

Figure 1 | Structural and chemical characterizations of CoO nanoparticles. a, Transmission electron micrograph. **b**, SAED pattern. **c**, X-ray photoemission spectra of CoO and Co_3O_4 micropowders.

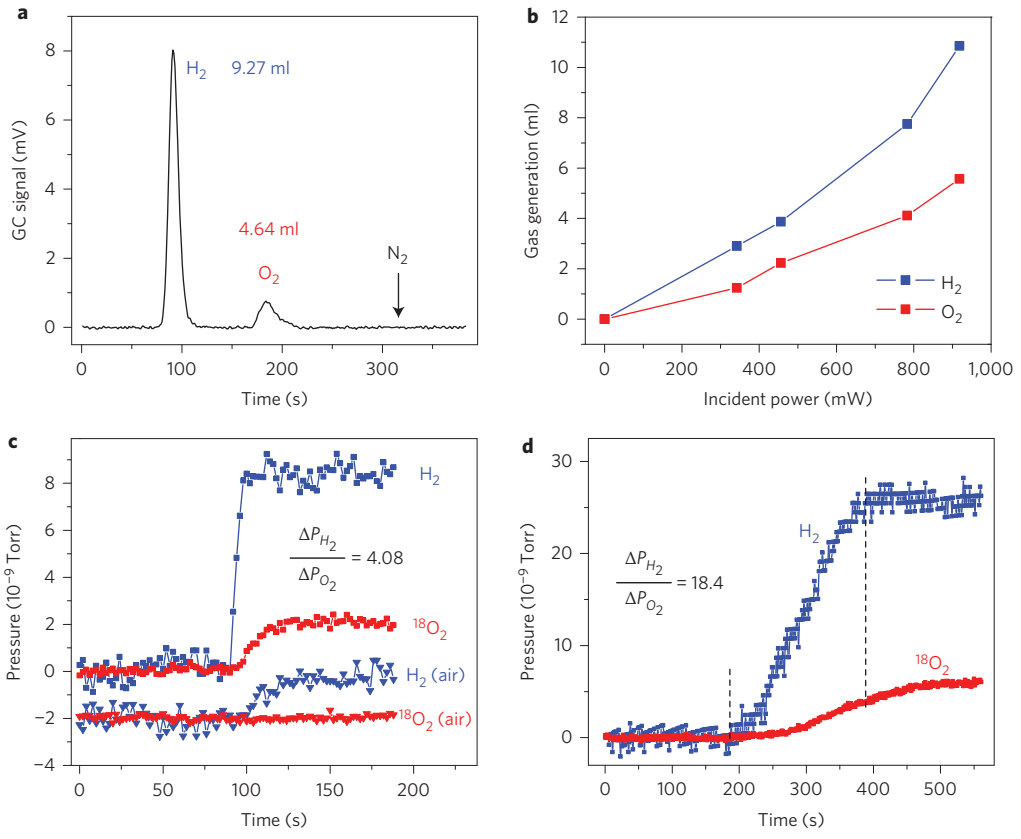

Figure 2 | Characterizations of hydrogen and oxygen evolutions with gas chromatography and mass spectrometry. a, A typical GC trace of evolved hydrogen and oxygen. **b**, Production of hydrogen and oxygen from CoO nanoparticles (~12 mg) as a function of incident laser power. The laser wavelength is 532 nm. **c**,**d**, Generation of H_2 and $^{36}O_2$ using ^{18}O-labelled water. The curves are shifted vertically for clarity. **c**, Pressure evolution of H_2 and $^{36}O_2$ after the gas sample (1 ml) was injected into the mass spectrometer. The upper two curves show gas from the photocatalytic reaction. The lower two curves are from air. **d**, Pressure evolution of H_2 and $^{36}O_2$ when ^{18}O-labelled water was electrolysed. The two dashed vertical lines mark the beginning and end of water electrolysis.

traces, we calibrated the response of the system with a fixed 2:1 ratio of H_2 to $^{36}O_2$. Basically, we used electrolysis to split the same $H_2^{18}O$ and monitored the gas production *in situ* with the mass spectrometer. Figure 2d shows RGA pressure traces for both H_2 and $^{36}O_2$ with ~4.18 as the pressure-change ratio of H_2 to $^{36}O_2$. This value is very close to the observed ratio of 4.08 in Fig. 2c, which implies a similar ratio of H_2 to $^{36}O_2$ in photocatalytic water-splitting as in water electrolysis. A nearly 2:1 ratio of H_2 to $^{36}O_2$ was also obtained by GC analysis, which further confirms a stoichiometric splitting of water.

The conclusion of CoO nanoparticle photocatalytic water-splitting is also supported by the following observations. There was no apparent change in the pH (6.7–6.9) of water before and after the reaction, which is an indication of stoichiometric decomposition of pure water because a non-stoichiometric generation of H_2 and O_2 will change the balance between OH^- and H^+ concentrations in water. We also repeated the same experiment with CoO micropowders (2–3 g), and no water splitting was observed. This observation agrees with theoretical predictions and confirms that bulk CoO is not a suitable photocatalyst because its conduction-band edge is located more than 600 mV below the hydrogen-evolution potential[17]. This observation also implies that the generation of hydrogen and oxygen cannot be explained by simple enhancement of the surface area of the nanocrystals relative to that of bulk CoO micropowders.

Nanotechnology has been regarded as an important means to modify a material's optical and electrochemical properties[18]. Owing to quantum confinement, typically nanostructures have larger bandgaps than the corresponding bulk materials. As a result, the absolute potentials of conduction- and valence-band edges have to be adjusted. An up-shift of the edge positions of the conduction band is observed in nanostructures such as α-Fe_2O_3 and CdSe quantum dots[19–21]. To understand the difference in catalytic activity between CoO nanocrystals and micropowders and to investigate the quantum size effect on the reactivity of CoO nanocrystals, we measured their bandgaps using diffuse reflectance spectroscopy[9,22,23]. Figure 3a shows the reflectivity spectra of both samples. The corresponding bandgaps were obtained from the corresponding modified Kubelka–Munk function, as shown in Fig. 3b[22]. It can be seen that CoO nanocrystals have a slightly lower bandgap than bulk CoO powders, which is in agreement with their lower reflectance in Fig. 3a. However, the two bandgaps are very close to 2.6 eV, a value similar to that reported in the literature[13,14,24]. This lack of a quantum-confinement effect probably results from the relatively large size (5–8 nm) of CoO nanoparticles[25]. The other absorption band edge near 2 eV is caused by the transition of electrons from the *d* band of Co^{2+} to the conduction band of CoO[26].

Surface states or morphology of nanostructures can also affect the band-edge positions of a material[27]. To obtain absolute band-edge positions with respect to water redox potentials, we fabricated CoO thin-film electrodes on fluorinated tin oxide glass using CoO nanocrystals and micropowders and measured their flat-band potentials[23,28]. Figure 3c shows the Mott–Schottky plots of both films—that is, $1/C^2$ as a function of electrochemical potentials, where the capacitance *C* was obtained from the impedance measurement. Unlike for the bandgap, a significant difference in the flat-band potentials between nanocrystals and micropowders was

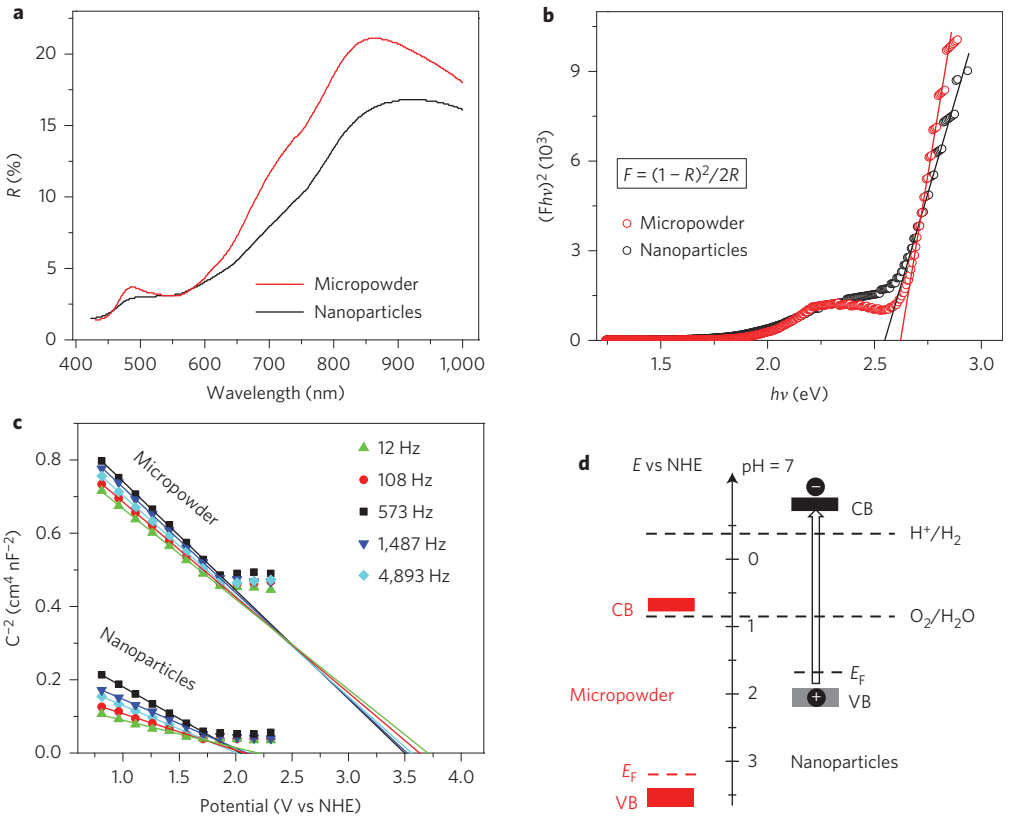

Figure 3 | Bandgaps and band-edge positions of CoO nanoparticles and micropowders. a, Ultraviolet–visible diffuse reflectance spectra of CoO nanocrystals and powders. **b**, $(Fh\nu)^2$ as a function of photon energy ($h\nu$), where *F* is the Kubelka–Munk function of the diffuse reflectance *R* from **a**. The intercepts of extrapolated straight lines give the corresponding direct bandgaps of CoO nanocrystals and powders. **c**, Mott–Schottky plots for CoO nanocrystals and micropowders according to impedance measurements. The flat-band potentials are obtained from the intercepts of the extrapolated lines. **d**, Band positions of CoO nanocrystals and micropowders according to the bandgaps and flat-band potentials obtained from **c**. CB, conduction band; VB, valence band.

observed, with the flat-band potential of CoO nanocrystals less than that of powders by more than 1 V. Negative slopes of Mott–Schottky plots indicate that CoO is *p*-type, which is believed to be the result of oxygen excess[13].

Figure 3d shows the approximate band-edge positions of both nanocrystals and micropowders based on the above-measured flat-band potentials, which are the differences between Fermi levels and water-reduction potential. Here we assumed that Fermi levels were about 0.3 eV above the valence bands for lightly doped *p*-type CoO[28,29]. Despite a lack of the precise value of the position of the Fermi level in the bandgap, important conclusions can be drawn from the energy diagram in Fig. 3d. As can be seen, a qualitative difference exists between nanocrystals and micropowders in their band-edge positions with regard to water redox potentials. In agreement with previous theoretical calculations, the edge position of the conduction band of CoO micropowders is located below the hydrogen-evolution potential, which indicates why the powders are not photocatalytically active for water splitting. In contrast, the conduction-band edge of CoO nanocrystals rises above the hydrogen-evolution potential, and the band edge of the valence band lies below the oxygen-evolution potential. This band alignment of CoO nanocrystals with water redox potentials explains why nanocrystals have significantly different photocatalytic activity to those of micropowders—it satisfies the necessary requirement for overall water splitting.

One of the most important factors to limit the solar-to-fuel application is its low conversion efficiency. As most photocatalysts can respond only to ultraviolet light, their solar-to-hydrogen efficiency is not reported frequently. The recently reported efficiency of white-light water-splitting devices is about 0.1%[6,7], which is far less than the efficiency of commercial photovoltaic cells. To obtain solar-to-hydrogen efficiency, we loaded CoO nanoparticles (~25 mg) in a flask and illuminated the particles with the AM1.5G simulated sunlight (100 mW cm^{-2}). After 30 minutes of illumination, an average of 20 ml H_2 was obtained, which corresponds to 210 J free energy. The total incident power over the 19 cm^2 bottom of the flask was 1.9 W, so the total input energy over 30 minutes was 3,420 J. A solar-to-hydrogen efficiency of ~5% was obtained, assuming all incident light was absorbed by optically thick nanoparticle suspension. This efficiency is 50 times larger than before, and is comparable to the efficiency achieved with artificial leaf based on the integration of three junction solar cells and optimized hydrogen- and oxygen-evolution catalysts[8].

As with many single-component photocatalysts, CoO nanoparticles also suffer from a short lifetime—they become deactivated after about one hour of reaction. X-ray diffraction and TEM diffraction spectra (Supplementary Figs 5 and 6) indicate that deactivated nanoparticles remain as CoO single crystals. However, the TEM image in Supplementary Fig. 6 reveals that the deactivated nanoparticles become aggregated and do not exhibit the sharp facets shown in Fig. 1a. The XPS in Supplementary Fig. 7 also shows a deviation of the spectrum from that of fresh CoO nanoparticles (shown in Fig. 1c). These preliminary studies indicate that the surfaces of CoO nanoparticles were corroded or oxidized. However, further investigation is needed to obtain a clear picture of the exact microscopic changes to their surface chemistry and lattice structure. We believe that, with further research, the deactivation can be reduced or eliminated, for example, by integrating CoO nanoparticles with suitable co-catalysts or other nanostructures[16].

According to conventional wisdom in the field, a highly active water-splitting particulate system requires an intimate integration of a suitable semiconductor particle with separate hydrogen- and oxygen-evolution co-catalysts[1,2,8,16] because such structures will reduce the water-splitting back-reaction and take advantage of the unique catalytic and optical properties of individual components of the system. The discovery of a highly active photocatalyst based on CoO nanoparticles provides an opportunity to develop practical solar fuel applications and gain new microscopic insights into photocatalytic water-splitting. Furthermore, despite the surprising catalytic property of CoO nanoparticles, Co-based catalysts are an emerging nanomaterial for oxygen evolution[8,30], hydrogen evolution[31] and artificial photosynthesis[32]. Our discovery adds to the growing potential of Co-based photocatalysts, and is expected to accelerate the pace of development of next-generation solar-fuel photocatalysts.

Received 28 May 2013; accepted 12 November 2013; published online 15 December 2013

References

1. Chen, X. B., Shen, S. H., Guo, L. J. & Mao, S. S. Semiconductor-based photocatalytic hydrogen generation. *Chem. Rev.* **110,** 6503–6570 (2010).
2. Kudo, A. & Miseki, Y. Heterogeneous photocatalyst materials for water splitting. *Chem. Soc. Rev.* **38,** 253–278 (2009).
3. Osterloh, F. E. & Parkinson, B. A. Recent developments in solar water-splitting photocatalysis. *Mater. Res. Soc. Bull.* **36,** 17–22 (2011).
4. Mallouk, T. E. The emerging technology of solar fuels. *J. Phys. Chem. Lett.* **1,** 2738–2739 (2010).
5. Walter, M. G. *et al.* Solar water splitting cells. *Chem. Rev.* **110,** 6446–6473 (2010).
6. Mubeen, S. *et al.* An autonomous photosynthetic device in which all charge carriers derive from surface plasmons. *Nature Nanotech.* **8,** 247–251 (2013).
7. Liu, C., Tang, J., Chen, H. M., Liu, B. & Yang, P. A fully integrated nanosystem of semiconductor nanowires for direct solar water splitting. *Nano Lett.* **13,** 2989–2992 (2013).
8. Nocera, D. G. The artificial leaf. *Acc. Chem. Res.* **45,** 767–776 (2012).
9. Maeda, K., Teramura, K. & Domen, K. Effect of post-calcination on photocatalytic activity of $(Ga_{1-x}Zn_x)(N_{1-x}O_x)$ solid solution for overall water splitting under visible light. *J. Catal.* **254,** 198–204 (2008).
10. Shi, H. G. & He, X. M. Large-scale synthesis and magnetic properties of cubic CoO nanoparticles. *J. Phys. Chem. Solids* **73,** 646–650 (2012).
11. Yin, J. S. & Wang, Z. L. Ordered self-assembling of tetrahedral oxide nanocrystals. *Phys. Rev. Lett.* **79,** 2570–2573 (1997).
12. Yang, H. M., Ouyang, J. & Tang, A. D. Single step synthesis of high-purity CoO nanocrystals. *J. Phys. Chem. B* **111,** 8006–8013 (2007).
13. Barreca, D. *et al.* Controlled vapor-phase synthesis of cobalt oxide nanomaterials with tuned composition and spatial organization. *CrystEngComm* **12,** 2185–2197 (2010).
14. Gallant, D., Pezolet, M. & Simard, S. Optical and physical properties of cobalt oxide films electrogenerated in bicarbonate aqueous media. *J. Phys. Chem. B* **110,** 6871–6880 (2006).
15. Grimblot, J., Bonnelle, J. P. & Beaufils, J. P. ESCA study on cobalt and molybdenum deposited on alumina – quantitative-analysis of recovery and states of specific cation adsorption. *J. Electron Spectrosc. Relat. Phenom.* **8,** 437–447 (1976).
16. Amirav, L. & Alivisatos, A. P. Photocatalytic hydrogen production with tunable nanorod heterostructures. *J. Phys. Chem. Lett.* **1,** 1051–1054 (2010).
17. Xu, Y. & Schoonen, M. A. A. The absolute energy positions of conduction and valence bands of selected semiconducting minerals. *Am. Miner.* **85,** 543–556 (2000).
18. Vayssieres, L. *et al.* One-dimensional quantum-confinement effect in α-Fe_2O_3 ultrafine nanorod arrays. *Adv. Mater.* **17,** 2320–2323 (2005).
19. Wang, H. L. & Turner, J. A. Characterization of hematite thin films for photoelectrochemical water splitting in a dual photoelectrode device. *J. Electrochem. Soc.* **157,** F173–F178 (2010).
20. Markus, T. Z. *et al.* Electronic structure of CdSe nanoparticles adsorbed on Au electrodes by an organic linker: Fermi level pinning of the HOMO. *J. Phys. Chem. C* **113,** 14200–14206 (2009).
21. Frame, F. A. *et al.* First demonstration of CdSe as a photocatalyst for hydrogen evolution from water under UV and visible light. *Chem. Commun.* 2206–2208 (2008).
22. McCarthy, T. J., Tanzer, T. A. & Kanatzidis, M. G. A new metastable 3-dimensional bismuth sulfide with large tunnels – synthesis, structural characterization, ion-exchange properties, and reactivity of KBi_3S_5. *J. Am. Chem. Soc.* **117,** 1294–1301 (1995).
23. Ishikawa, A. *et al.* Oxysulfide $Sm_2Ti_2S_2O_5$ as a stable photocatalyst for water oxidation and reduction under visible light irradiation ($\lambda \leq 650$ nm). *J. Am. Chem. Soc.* **124,** 13547–13553 (2002).
24. Mane, A. U. & Shivashankar, S. A. MOCVD of cobalt oxide thin films: dependence of growth, microstructure, and optical properties on the source of oxidation. *J. Cryst. Growth* **254,** 368–377 (2003).
25. Holmes, M. A., Townsend, T. K. & Osterloh, F. E. Quantum confinement controlled photocatalytic water splitting by suspended CdSe nanocrystals. *Chem. Commun.* **48,** 371–373 (2012).

26. Johnson, C. A. *et al.* Visible-light photoconductivity of $Zn_{1-x}Co_xO$ and its dependence on Co^{2+} concentration. *Phys. Rev. B* **84,** 125203 (2011).
27. Jasieniak, J., Califano, M. & Watkins, S. E. Size-dependent valence and conduction band-edge energies of semiconductor nanocrystals. *ACS Nano* **5,** 5888–5902 (2011).
28. Pinaud, B. A., Chen, Z. B., Abram, D. N. & Jaramillo, T. F. Thin films of sodium birnessite-type MnO_2: optical properties, electronic band structure, and solar photoelectrochemistry. *J. Phys. Chem. C* **115,** 11830–11838 (2011).
29. Matsumoto, Y. Energy positions of oxide semiconductors and photocatalysis with iron complex oxides. *J. Solid State Chem.* **126,** 227–234 (1996).
30. Riha, S. C. *et al.* Atomic layer deposition of a submonolayer catalyst for the enhanced photoelectrochemical performance of water oxidation with hematite. *ACS Nano* **7,** 2396–2405 (2013).
31. Marinescu, S. C., Winkler, J. R. & Gray, H. B. Molecular mechanisms of cobalt-catalyzed hydrogen evolution. *Proc. Natl Acad. Sci. USA* **109,** 15127–15131 (2012).
32. Jiao, F. & Frei, H. Nanostructured cobalt oxide clusters in mesoporous silica as efficient oxygen-evolving catalysts. *Angew. Chem. Int. Ed.* **48,** 1841–1844 (2009).

Acknowledgements

Financial support from the Robert A. Welch Foundation (E-1728), National Science Foundation (DMR 0907336) and Department of Energy (DE-FG02-13ER46917) is acknowledged. We thank J. Shan and P. Tian for assistance with the purchase of the femtosecond laser, M. Shen, J. Deng, R. Thummel, R. Zhong, H. Fang, Z. Tang, D. Achey, X. Ni, J. Sun, X. Ren, Y. Qi, S Pei, J. Zhao, P. Ruchhoeft, Q. Zhang and J. Allen for help and valuable discussions, and Z. Liu, X. Gong, P. Peng, P. Zhu and M. Fang for various contributions.

Author contributions

L.L. and J.M.B. conceived, designed and performed the experiments, and analysed the data. D.W. and F.R-H. performed TEM studies, Q.Z. and Y.L. performed ultraviolet–visible measurements, S.B. and X.C. helped design and fabricate reaction chambers, and assisted in electrochemical studies, Q.Y, J.Z. and G.F. assisted in laser ablation, Z.R. and H.F. assisted in ball-milling synthesis, Z.S., Z.Z., Y.W. and X.L. assisted in mass spectrometry, gas chromatography, SEM studies and the solar-simulator set-up, J.M.B. wrote the manuscript and prepared the figures. All authors discussed the results and commented on the manuscript. J.M.B. supervised the project.

Additional information

Supplementary information is available in the online version of the paper. Reprints and permissions information is available online at www.nature.com/reprints. Correspondence and requests for materials should be addressed to J.B.

Competing financial interests

The authors declare no competing financial interests.